



**Orientation loss of microcrystals of DyBa<sub>2</sub>Cu<sub>3</sub>O<sub>y</sub> in polymer composite during curing of the medium under an external magnetic field**

Journal:	<i>CrystEngComm</i>
Manuscript ID	CE-ART-06-2020-000795.R1
Article Type:	Paper
Date Submitted by the Author:	18-Jul-2020
Complete List of Authors:	Kimura, Tsunehisa; Kyoto University; Fukui University of Technology Kashiwagi, Hayato ; Kyoto University - Yoshida Campus Kimura, Fumiko; Kyoto University of Advanced Science, Horii, Shigeru; Kyoto University of Advanced Science Takeda, Kazuki ; Kyoto University Graduate School of Science Faculty of Science Doi, Toshiya; Kyoto University - Yoshida Campus

## ARTICLE

# Orientation loss of microcrystals of DyBa<sub>2</sub>Cu<sub>3</sub>O<sub>γ</sub> in polymer composite during curing of the medium under an external magnetic field

Received 00th January 20xx,  
Accepted 00th January 20xx

DOI: 10.1039/x0xx00000x

Tsune-hisa Kimura,<sup>\*a,b</sup> Hayato Kashiwagi,<sup>c</sup> Fumiko Kimura,<sup>d</sup> Shigeru Horii,<sup>d</sup> Kazuki Takeda,<sup>e</sup> and Toshiya Doi<sup>c</sup>

A liquid medium containing microcrystals of DyBa<sub>2</sub>Cu<sub>3</sub>O<sub>γ</sub> with γ~7 (Dy123) was cured under a magnetic field, and the change in crystal orientation during the curing was monitored by means of in-situ X-ray diffraction measurement. The initially achieved crystal orientation deteriorated as curing proceeded. We present a model that explains the experimental results. The model showed that the orientation loss depends on particle size, degree of shrinkage, initial viscosity of the matrix, and cure rate. We found that there is an optimum condition that minimizes the deterioration of orientation.

## Introduction

Magnetic orientation of fillers such as microcrystals<sup>1,2</sup>, whiskers<sup>3</sup>, fibers<sup>4,5</sup>, nanotubes<sup>6-8</sup>, etc. in composite is a powerful means to improve the physical properties of the composite. To prepare oriented composites, a suspension of the filler is exposed to a magnetic field and the medium is cured by irradiation of light, heating, etc. to consolidate the crystal orientation. In our experience, the orientation achieved in a liquid medium partially deteriorates during the curing of the medium, even though the magnetic field is maintained until the consolidation is complete. This impairs the quality of the final product.

Furthermore, the high orientation of the microcrystal is particularly important when the oriented composite is used for single crystal X-ray diffraction (XRD) analysis<sup>9-12</sup> and the single-crystal solid-state nuclear magnetic resonance (NMR)<sup>13</sup> of the microcrystal contained in the composite. The deterioration of orientation during the consolidation process hinders successful

analyses in these experiments.

There are a number of studies on curing resins,<sup>14,15</sup> but very little is known about the mechanism of the orientation deterioration. In this paper, we perform in-situ X-ray diffraction measurement of the suspension of microcrystalline powder of DyBa<sub>2</sub>Cu<sub>3</sub>O<sub>γ</sub> with γ~7 (Dy123)<sup>16</sup> in an adhesive exposed to a magnetic field<sup>17</sup> to study the mechanism of the orientation loss during the curing. Dy123 is paramagnetic and exhibits a quick response to the magnetic field,<sup>18</sup> which facilitates the in-situ measurement required in this study. The magnetic orientation of Dy123 microcrystals is of interest in itself to enhance its superconducting property. The experimental data is explained by a theoretical model of consolidation.

## Results and discussion

### Magnetic orientation of the biaxial crystal under a rotating magnetic field

Let us consider a biaxial crystal (orthorhombic, monoclinic, triclinic) suspended in a matrix of liquid resin precursor. The anisotropic magnetic susceptibility of the crystal is defined by three principal values,  $\chi_1$ ,  $\chi_2$ , and  $\chi_3$ , and the corresponding principal axes of its magnetic susceptibility tensor (Fig. 1). Here, we define the values as  $\chi_1 > \chi_2 > \chi_3$ .

When this crystal is exposed to a magnetic field  $B$  uniformly rotating in the  $xy$  plane with the rotation speed of  $\omega$ , the magnetic energy acquired by the crystal is expressed by

<sup>a</sup> Fukui University of Technology, 3-6-1 Gakuen, Fukui 910-8505, Japan.

<sup>b</sup> Kyoto University, Sakyo-ku, Kyoto 606-8502, Japan.

<sup>c</sup> Graduate School of Energy Science, Kyoto University, Yoshida-Honmachi, Sakyo-ku, Kyoto 606-8501, Japan.

<sup>d</sup> Nagamori Institute of Actuators, Kyoto University of Advanced Science, Yamanouchi-Gotandacho, Ukyo-ku, Kyoto 615-8577, Japan.

<sup>e</sup> Division of Chemistry, Graduate School of Science, Kyoto University, Kyoto 606-8502, Japan.

† Footnotes relating to the title and/or authors should appear here.

Electronic Supplementary Information (ESI) available: [details of any supplementary information available should be included here]. See DOI: 10.1039/x0xx00000x

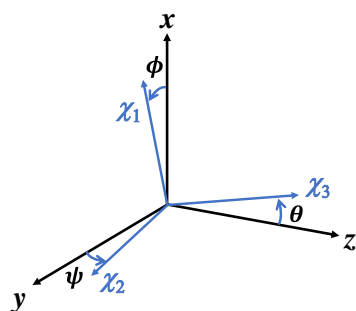


Fig. 1 Orientation of magnetic axes,  $\chi_1$ ,  $\chi_2$ , and  $\chi_3$ , with respect to the laboratory coordinates  $x$ ,  $y$ , and  $z$  defined by Euler angles,  $\phi$ ,  $\theta$ , and  $\psi$ . Euler angles are assumed to be small.

$$E_{\text{mag}} = \frac{(\chi_1 - \chi_3)VB^2}{4\mu_0}\theta^2 + \frac{(\chi_2 - \chi_3)VB^2}{4\mu_0}\psi^2, \quad (1)$$

where  $V$  is the volume of the crystal,  $B$  is the intensity of magnetic field, and  $\mu_0$  is the magnetic permeability of the vacuum.<sup>9</sup> Euler angles  $\theta$  and  $\psi$  are defined in Fig. 1. The angle  $\phi$  does not occur in the energy because there is a freedom of rotation about the  $z$  axis. Here, isotropic and higher terms are disregarded. The equation for the magnetic energy indicates that  $\theta = \psi = 0$  is a stable state, that is, the  $\chi_3$  axis aligns in the  $z$ -axis.

In the equilibrium state, the mean square fluctuations  $\langle\psi^2\rangle_0$  and  $\langle\theta^2\rangle_0$  (rad<sup>2</sup>) around the minimum due to the Brownian motion are expressed by

$$\langle\theta^2\rangle_0 = \frac{2k_B T \mu_0}{(\chi_1 - \chi_3)VB^2}$$

and

$$\langle\psi^2\rangle_0 = \frac{2k_B T \mu_0}{(\chi_2 - \chi_3)VB^2}, \quad (2)$$

where  $k_B$  is the Boltzmann constant and  $T$  is the temperature. Suffix 0 indicates that the consolidation process does not begin yet. In the present study, we monitor these fluctuations through the FWHMs of diffraction spots appearing at almost identical diffraction angles (see Experimental). Then we introduce the observed square FWHM as follows:

$$\langle\beta^2\rangle_0 = \frac{1}{2}(\langle\theta^2\rangle_0 + \langle\psi^2\rangle_0) = \frac{2k_B T \mu_0}{\chi_a VB^2}, \quad (3)$$

where  $\chi_a^{-1} \equiv (1/2)((\chi_1 - \chi_3)^{-1} + (\chi_2 - \chi_3)^{-1})$ .

### Model for the deterioration of orientation under consolidation process

A model for the effect of the consolidation of the matrix resin precursor on the deterioration of orientation is proposed. It is assumed that the magnetic orientation is achieved before substantial consolidation begins. The matrix resin precursor begins to undergo a chemical reaction upon irradiation with ultra violet light, heating, etc. We assume that the curing process itself is not affected by the magnetic field. The decrease in volume takes place at sites of the medium where

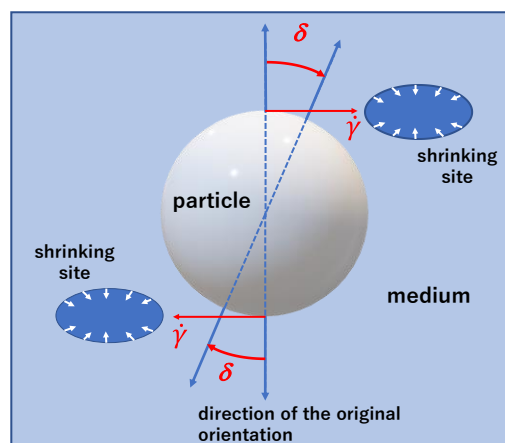


Fig. 2 Local shear strain (LSS) model. The chemical reaction that occurs inhomogeneously in the medium causes shrinking sites in the vicinity of the particle. As a result, shearing strain is generated around the particle, causing the particle to rotate from its original orientation. The degree of rotation depends on the correlation between the shrinking sites and the original orientation axis of the particle. For example, if the shrinking sites are collinear with the orientation axis, the orientation does not change. If the shrinking sites are arranged as shown in the figure, shear strain is applied to the particle, and the orientation changes by the angle  $\delta$ . As a result, the work is exerted on the medium. The value of  $\delta$  vanishes when the shrinking sites are collinear with the orientation axis and up to  $\pi/2$  when the two shrinking sites are arranged perpendicular to the orientation axis.

the chemical reaction occurs, causing a local shear strain (LSS) around the particles. As a result, a rotational motion of the particle (Fig. 2) is induced, which exerts the work on the medium. The work exerted is expressed by<sup>19</sup>

$$\Delta E_{\text{LSS}} = 8\pi a^3 \eta \dot{\gamma} \delta, \quad (4)$$

where  $\eta$  is the viscosity of the medium and  $\dot{\gamma}$  is the rate of the change in the local shear strain  $\gamma$ . Here, we assume that the particle is spherical and that  $a$  is the radius of the sphere. Since we cannot know the LSS detail, the change  $\delta$  in orientation of the particle is unknown. Here, we simply suppose  $\delta = 1$  because  $0 < \delta < \pi/2$ . Then the total energy of the particle is expressed by

$$\begin{aligned} \Delta F &= \Delta E_{\text{mag}} - \Delta E_{\text{LSS}} \\ &= \frac{(\chi_1 - \chi_3)VB^2}{4\mu_0}\theta^2 + \frac{(\chi_2 - \chi_3)VB^2}{4\mu_0}\psi^2 - 8\pi a^3 \eta \dot{\gamma}, \end{aligned} \quad (5)$$

Using this expression, we obtain

$$\langle\theta^2\rangle_{\text{mag}} = \langle\theta^2\rangle_0 G(t) \text{ and } \langle\psi^2\rangle_{\text{mag}} = \langle\psi^2\rangle_0 G(t), \quad (6)$$

where  $G(t)$  is defined by

$$G(t) = \exp\left(\frac{\Delta E_{\text{LSS}}}{k_B T}\right) = \exp\left(\frac{8\pi a^3 \eta \dot{\gamma}}{k_B T}\right).$$

(7)

Using eq. (3), we obtain

$$\langle \beta^2 \rangle_{\text{obs}} \equiv \frac{1}{2} (\langle \theta^2 \rangle_{\text{mag}} + \langle \psi^2 \rangle_{\text{mag}}) = \langle \beta^2 \rangle_0 G(t). \quad (8)$$

We assume that the local shear strain  $\gamma$  may be replaced with a macroscopic strain, which we express by a sigmoid function expressed by

$$\gamma = \frac{\gamma_{\infty}}{1 + \exp\left(-\frac{t + t_0}{\tau_s}\right)}, \quad (9)$$

where  $t$  is the consolidation time,  $\tau_s$  is a time constant for shrinkage, and  $t_0$  is an adjustable parameter.  $\gamma$  is an increasing function of  $t$ , beginning with zero and reaching  $\gamma_{\infty}$ . For example, if the macroscopic shrinkage is 5%,  $\gamma_{\infty} = 0.05$ . We also assume that the temporal change in viscosity  $\eta$  is expressed by<sup>14</sup>

$$\eta = \eta_0 \left(1 + \exp\left(\frac{t + t_0}{\tau_{\eta}}\right)\right). \quad (10)$$

Here,  $\eta_0$  is the initial viscosity of the suspending medium and  $\tau_{\eta}$  is a time constant for the increase in viscosity.

Then eq. (7) is expressed by

$$G(t) = \exp\left[K \left(1 + e^{\frac{t+t_0}{\tau_{\eta}}}\right) \left(1 + e^{\frac{t+t_0}{\tau_s}}\right)^{-2} e^{\frac{t+t_0}{\tau_s}}\right], \quad (11)$$

where

$$K = \frac{8\pi a^3 \eta_0 \gamma_{\infty}}{k_B T \tau_s} = \frac{\gamma_{\infty}}{D_{\text{rot}} \tau_s}. \quad (12)$$

Here,  $D_{\text{rot}} = k_B T / 8\pi a^3 \eta_0$  is the rotational diffusion constant of the particle (Stokes–Einstein–Debye law) in the medium before solidification. The parameter  $K$  is the ratio of the two kinetic factors,  $D_{\text{rot}}$  and  $\gamma_{\infty} / \tau_s$ . These two factors are competing. The former is the speed at which the memory of orientation disappears, and the latter is the rate of deformation. Qualitatively, a large  $K$  indicates that the deformation rate dominates over the relaxation of the induced orientation. On the other hand, a small  $K$  indicates that the induced orientation relaxes faster than deformation.  $K = 1$  is the point where these two opposite kinetics balances.

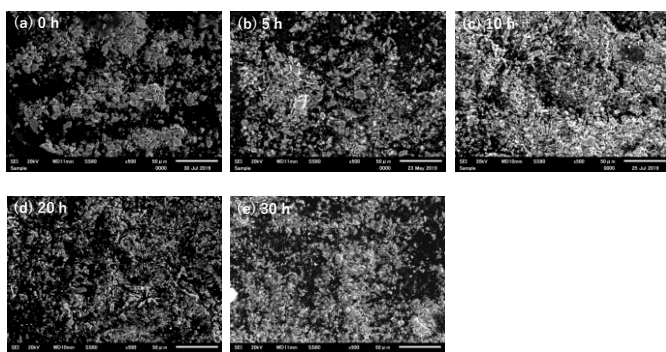


Fig. 3 SEM microphotographs of Dy123 powder samples. Ball-milling time is (a) 0 h, (b) 5 h, (c) 10 h, (d) 20 h, and (e) 30 h. Size bar is 50  $\mu\text{m}$ .

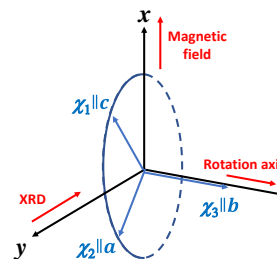


Fig. 4 Experimental setup of the sample rotation and X-ray beam setting. The capillary is rotated about the z-axis (horizontal) to which the  $b$  axis aligns. The  $a$  and  $c$  axes are distributed uniformly in the  $xy$  plane (vertical) because, in this experimental setting, there is freedom of rotation about the  $b$  axis.

If  $\tau_{\eta} = \tau_s$ , which is approximately valid in the present experiment as we will find later in the fitting procedure, then,  $G(t)$  is simplified as

$$G(t) = \exp\left(\frac{K}{1 + \exp\left(-\frac{t + t_0}{\tau_s}\right)}\right), \quad (13)$$

where  $K$  is given by eq. (12). We find that  $G(\infty)$  levels off at  $e^K$ . This value is small when  $K$  is small. Then the level-off value of  $\langle \beta^2 \rangle_{\text{obs}}$  is expressed by

$$\langle \beta^2 \rangle_{\text{obs}}^{\infty} \equiv \langle \beta^2 \rangle_0 G(\infty) = (p/K)e^K, \quad (14)$$

where  $p = 12\mu_0\eta_0\gamma_{\infty}/(\chi_a B^2 \tau_s)$ . We find that the above equation has a minimum at  $K = 1$ . This indicates that in order to reduce the disorientation, the sample size should be smaller when  $K > 1$ , and it should be larger when  $K < 1$ .

So far, we have assumed that the particle shape is spherical. In many cases, it is not. If the shape is prolate or oblate, eq. (4) should be modified to  $\Delta E_{\text{LSS}} = 8\pi a^3 \eta \dot{\gamma} D / F(D)$ , where  $a$  and  $D$  are the radius and the aspect ratio, respectively, of the prolate or oblate shape. For a sphere,  $D = F(D) = 1$ . For a prolate shape,  $D > 1$ , and for the oblate shape  $D < 1$ . The function  $F(D)$  is reported elsewhere.<sup>20–22</sup> Furthermore, the rotation is more complicated for nonspherical particles. For example, there are two types of rotations for a rod-like particle: the rotation about the rod axis and the rotation about the axis perpendicular to the rod axis. The former might contribute to  $\Delta E_{\text{LSS}}$  less than the latter. The microcrystals of Dy123 used in this study look oblate, but the shape effect was not considered in this study. The shape effect should be considered for more detailed analyses.

### Experimental results and fitting

In Fig. 3, SEM microphotographs of the samples (ball mill treatment time of 0, 5, 10, 20, and 30 h) are shown. The crystal size was not determined exactly, but we find that the size becomes smaller with increased milling time.

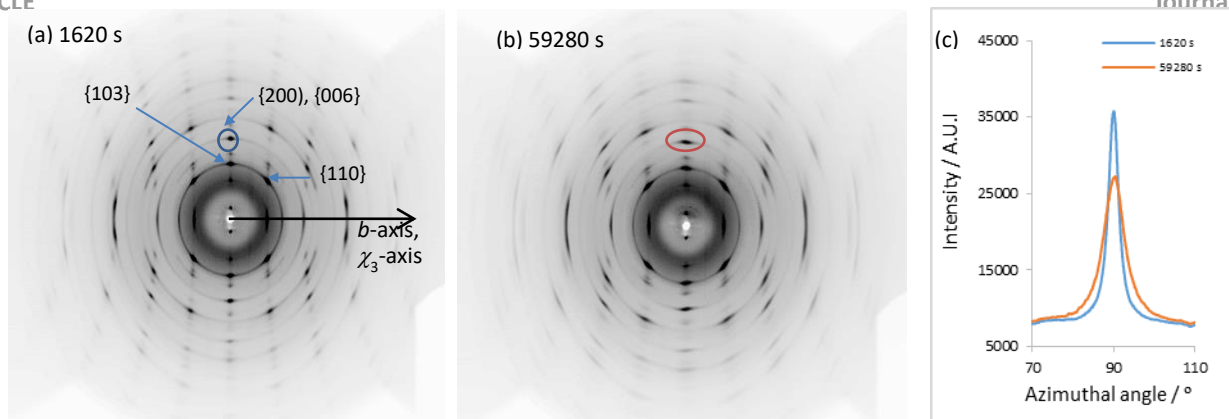


Fig. 5 2D XRD profiles of the sample (ball-milling time of 5 h) measured at a consolidation time of  $t = 1620$  (a) and  $59280$  s (b). Encircled spots at  $2\theta = 20.5\text{--}21.8^\circ$  in (a) and (b) are assigned to diffraction from the (200) and (006) planes. A diffuse ring is attributed to the matrix. The assignments for some spots are shown. (c) Azimuthal plot at  $2\theta = 20.5\text{--}21.8^\circ$  around the spots (azimuthal angle centered at  $90^\circ$ ) encircled in (a) and (b).

Since the Dy123 crystal is orthorhombic ( $Pmmm$  (47),  $a = 3.8244(1)\text{\AA}$ ,  $b = 3.8890(1)\text{\AA}$ ,  $c = 11.6885(3)\text{\AA}$ )<sup>16, 23</sup> there is a relationship<sup>24</sup> between its magnetic and crystallographic axes, described as  $\chi_1 \parallel c$ ,  $\chi_2 \parallel a$ , and  $\chi_3 \parallel b$ .<sup>17</sup> In the present experimental setup (Fig. 4), the capillary is rotated about the  $z$ -axis (horizontal), and hence the  $b$  axis aligns horizontally. On the other hand, the  $a$ - and  $c$ -axes are distributed uniformly in the  $xy$  plane (vertical) because there is a freedom of rotation about the  $b$  axis. It should be noted that the sample rotation is too fast for the  $\chi_1$  axis to be able to follow the magnetic field (Rapid Rotation Regime<sup>9</sup>). The X-ray is impinged from the  $y$ -axis. The (200) and (006) diffractions show up in the meridian.

Figure 5a and b show the 2D XRD pattern measured at two different consolidation times, and Fig. 5c shows the azimuthal  $\beta$  plots. The diffraction patterns are typical of magnetic orientation<sup>25</sup>. The patterns exhibit a fiber pattern where the equator is the fiber axis. We clearly observe the layered lines parallel to the meridian. The diffraction spots in the  $k^{\text{th}}$  layer are assigned to be  $(hkl)$ . In the  $0^{\text{th}}$  layer (meridian), the spots are assigned to  $(h0l)$ , which include (200) and (006). Since the  $d$ -spacings of (200) and (006) are almost the same (corresponding to  $21.42^\circ$  and  $21.02^\circ$ , respectively), the spots around  $21^\circ$  (marked by a circle in each of Figs. 5a and b) are assigned to the overlap of (200) and (006). With increase in consolidation time, the full width at half maximum (FWHM) of this spot increases. In Fig. 5c, the azimuthal plot around  $\beta = 90^\circ$  is shown. We used the FWHM of this peak to estimate the orientation disorder because the fluctuations  $\langle \theta^2 \rangle_0$  and  $\langle \psi^2 \rangle_0$  in eq. (2) are directly related to the FWHM of (006) and (200), respectively.

In Fig. 6, the square of the XRD full width at half maximum (FWHM)  $\langle \beta^2 \rangle_{\text{obs}}$  of five samples is plotted as a function of the consolidation time  $t$ . The value of  $\langle \beta^2 \rangle_{\text{obs}}$  begins with the equilibrium value of  $\langle \beta^2 \rangle_0$  and increases with the consolidation time  $t$ , which is in agreement with the theoretical prediction in eq. (8). Fitting was performed and the result is indicated by solid curves. The fitting shown in the figure was obtained by using all experimental data points. We also made fittings for which data points at a shorter  $t$  were removed because data points are scattered at a shorter  $t$  (see SI).

The parameters used for the fitting are summarized in Table 1. We find that  $\langle \beta^2 \rangle_0$  is proportional to the ball-milling time which is consistent with eq. (3). The values of  $\tau_s$  are scattered from sample to sample. This might be due to the difference in experimental procedures for mixing resin and hardener, which is difficult to control.  $\tau_\eta$  is almost identical with  $\tau_s$  for each sample. This indicates that the increase in viscosity proceeds at approximately the same time constant as the consolidation process. We find that  $\tau_\eta < \tau_s$  for the samples (\*0 h, \*5 h, \*10 h, \*20 h) whose values of  $\langle \beta^2 \rangle_{\text{obs}}$  monotonously increase, while  $\tau_\eta > \tau_s$  for the sample (\*30 h) whose value of  $\langle \beta^2 \rangle_{\text{obs}}$  decreases at a prolong  $t$ . This is consistent with the behavior of  $G(t)$  (eq. (11)).

Combining eqs. (3) and (12), we have a relationship between  $\langle \beta^2 \rangle_0$  and  $K^{-1}$ :

$$\langle \beta^2 \rangle_0 = \frac{12\mu_0\eta_0\gamma_\infty}{\tau_s\chi_a B^2} K^{-1}. \quad (15)$$

In Fig. 7,  $\langle \beta^2 \rangle_0$  is plotted as a function of  $K^{-1}$ . The slope  $0.0009 \text{ rad}^2$  should be compared to the proportionality constant,  $12\mu_0\eta_0\gamma_\infty/(\tau_s\chi_a B^2)$ , in eq. (15). This slope value gives rise to  $\chi_a = 1.4 \times 10^{-5}$  if we assign  $\eta_0 = 40 \text{ Pa s}$ ,<sup>26</sup>  $\gamma_\infty = 0.05$ ,<sup>27-30</sup>  $B = 1/\sqrt{2} \text{ T}$  (factor of  $\sqrt{2}$  because of sample rotation)  $\tau_s = 4,664 \text{ s}$  (average from Table 1), and  $\mu_0 = 4\pi \times 10^{-7} \text{ Wb/(A m)}$ . This value is about one order smaller than the reported value of  $\Delta\chi \cong 10^{-4}$ .<sup>18, 31</sup> It has been reported<sup>17, 32, 33</sup> that the Dy123 microcrystal forms a twin structure in which the (110) plane is shared so that the  $c(\parallel\chi_1)$  axes are antiparallel to each other. As a result,  $\chi_2 - \chi_3$  might be small. As defined previously,  $\chi_a^{-1} \equiv (1/2)((\chi_1 - \chi_3)^{-1} + (\chi_2 - \chi_3)^{-1})$ . Then, if  $\chi_2 - \chi_3$  is small compared to  $\chi_1 - \chi_3$ , we have  $\chi_a \cong 2(\chi_2 - \chi_3)$ . This could explain the small value of  $\chi_a = 1.4 \times 10^{-5}$  compared to  $\Delta\chi \cong 10^{-4}$  for the single-crystal Dy123. In Fig. 7, the intercept value  $\langle \beta^2 \rangle_{\text{obs}}$  is not zero but  $0.0018 \text{ rad}^2$ . This contradicts eq. (15). This residual value of  $0.0018 \text{ rad}^2$ , corresponding to the FWHM of  $2.4^\circ$ , might be attributed to the intrinsic disorder  $\langle \beta^2 \rangle_{\text{mos}}$  due to the crystal mosaicity. The experimentally observed fluctuation might be rewritten as

$$\langle \beta^2 \rangle_{\text{obs}} = \langle \beta^2 \rangle_{\text{mos}} + \langle \beta^2 \rangle_0 G(t). \quad (16)$$

Table 1 Parameters used for fitting for the 5 samples in Fig. 6 identified by ball-milling time, 0 h, 5 h, 10 h, 20 h, and 30 h. The first column with an asterisk indicates that the fitting was made using all experimental data points. The fittings for the data from 10 h, 20 h, and 30 h were not satisfactory because of the data point scattering. Then other fittings were performed using different sets of parameters, and these results are shown in SI.  $\langle \beta^2 \rangle_{\text{obs}}^{80,000}$  is the value of the fitting function at  $t = 80,000$ , which we regard as  $\langle \beta^2 \rangle_{\text{obs}}^{\infty}$ .

	$\langle \beta^2 \rangle_0 / \text{rad}^2$	$t_0 / (10^4 \text{ s})$	$\tau_{\eta} / (10^3 \text{ s})$	$\tau_s / (10^3 \text{ s})$	$K$	$\langle \beta^2 \rangle_{\text{obs}}^{\infty} / \text{rad}^2$ at 80,000 s
*0 h	0.0025	-1.29	3.07	3.08	1.49	0.0117
*5 h	0.0026	-1.06	3.71	3.72	1.44	0.0116
*10 h	0.0029	-0.97	8.14	8.19	0.57	0.0054
10 h (1)	0.0032	-1.18	7.38	7.43	0.50	0.0054
*20 h	0.0043	-1.58	3.11	3.14	0.33	0.0064
20 h (1)	0.0043	-1.50	5.18	5.24	0.34	0.0064
20 h (2)	0.0042	-1.40	5.76	5.82	0.37	0.0064
20 H (3)	0.0040	-1.18	7.06	7.12	0.42	0.0064
*30 h	0.0048	-1.51	5.75	5.64	0.39	0.0067
30 h (1)	0.0052	-1.55	2.26	2.28	0.25	0.0071
30 h (2)	0.0051	-1.52	2.66	2.67	0.27	0.0070
30 h (3)	0.0051	-1.54	2.83	2.82	0.29	0.0067
30 h (4)	0.0051	-1.56	3.52	3.49	0.31	0.0067

The value of  $2.4^\circ$  might be an overestimation of the actual mosaicity because the instrumental function of the X-ray diffractometer was not considered in the present analysis.

In Fig. 8,  $\langle \beta^2 \rangle_{\text{obs}}$  at  $t = 80,000$  s (denoted by  $\langle \beta^2 \rangle_{\text{obs}}^{80,000}$  which is actually regarded as  $\langle \beta^2 \rangle_{\text{obs}}^{\infty}$ ) is plotted as a function of  $K$ . We find that  $\langle \beta^2 \rangle_{\text{obs}}^{\infty}$  has a minimum at  $K \sim 1$  as predicted in eq. (14) although the data does not fit very well to the function form of  $(p/K)e^K$ . This observation supports the idea that  $\langle \beta^2 \rangle_{\text{obs}}^{\text{max}}$  can be minimized for a given sample size  $a$  by setting the experimental condition so that  $K =$

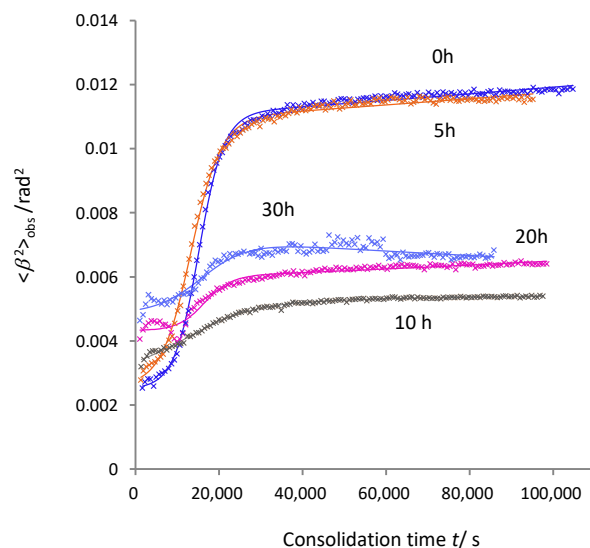


Fig. 6 The square of the XRD FWHM  $\langle \beta^2 \rangle_{\text{obs}}$  of five samples distinguished by the ball-milling time (0 h, 5 h, 10 h, 20 h, and 30 h) is plotted as a function of the consolidation time  $t$ . Symbols (x) are experimental data and solid curves are the results of fitting for which all data points are used. The parameters used for the fitting are summarized in Table 1.

$8\pi a^3 \eta_0 \gamma_{\infty} / (k_B T \tau_s) = 1$  is satisfied. If we assume that  $T = 300$  K,  $\tau_s \cong 4,664$  s,  $\eta_0 \cong 40$  Pa s, and  $\gamma_{\infty} \cong 0.05$ , we have  $a = 1.1 \mu\text{m}$  at the minimum. The samples between 5–10 h ball-milling time seem to give the value of  $K \sim 1$  (Table 1). The size of these samples observed in microphotographs (Fig. 3) should be compared with this calculated value of  $a$ . The size distribution of these samples is large, and exact comparison is difficult, but we may say that the order of the sizes is in agreement.

In the present experiment, the magnetic field is maintained during consolidation. Then the magnetic orientation competes with the disorientation by consolidation. If the time constant  $\tau_m$  of magnetic orientation is smaller than the time constant  $\tau_s$  of consolidation, the loss of orientation can be recovered. This condition is expressed by

$$\tau_m = \frac{6\mu_0\eta}{\chi_a B^2} \ll \tau_s. \quad (17)$$

If we assign  $\eta = \eta_0 = 40$  Pa s,  $\chi_a = 10^{-4}$ , and  $B = 1/\sqrt{2}$  T as we did previously, then we obtain  $\tau_m = 6.0$  s. Since  $\tau_s \cong 4,664$  s, eq. (17) is satisfied at an early stage of consolidation. When the consolidation proceeds,  $\eta$  increases, and the  $\tau_m$  becomes larger than the  $\tau_s$ . Then the mechanism described by the model described here begins dominant.

The consolidation may sometimes be performed after the magnetic field is removed. In such circumstances, two processes contribute to the loss of orientation, that is, the rotational diffusion at an early stage followed by the loss in orientation by the consolidation. As soon as the magnetic confinement is removed, the rotational diffusion begins, and the fluctuation will increase like  $D_{\text{rot}}t$  until the rotational diffusion constant  $D_{\text{rot}}$  vanishes due to the increase in viscosity, where  $t$  is the time elapsed before the viscosity begins to increase. On the other hand, the loss in orientation due to consolidation proceeds in a way described by  $G(t)$  shown in eq. (7).

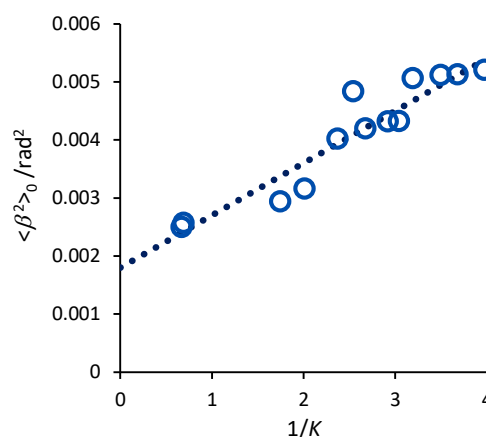


Fig. 7  $\langle \beta^2 \rangle_0$  is plotted as a function of  $1/K$  using the data in Table 1. Data points are fitted as a straight line with a slope of  $0.0009 \text{ rad}^2$  and a y-intercept of  $0.0018 \text{ rad}^2$ .

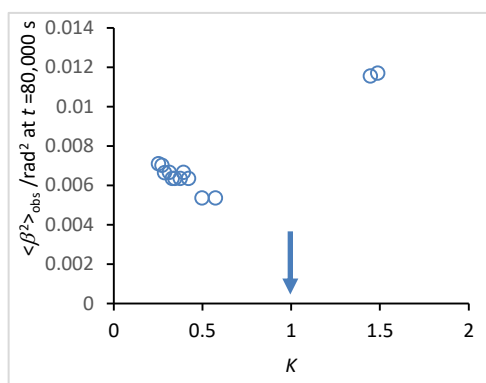


Fig. 8  $\langle \beta^2 \rangle_{\text{obs}}$  values at  $t = 80,000$  s taken from fitting curves are plotted as a function of  $K$ . A minimum seems to be located at  $K = 0.8$ – $1.2$ . The arrow indicates  $K = 1$  where the minimum is predicted by the model.

The deformation due to the shrinkage may be expressed by a shear strain field  $\mathbf{S} = (\omega y, 0, 0)$  (Fig. 9a). This strain field satisfies  $\text{rot } \mathbf{S} \neq 0$ , indicating that the particle in this field rotates, resulting in orientation deterioration. Another possible strain field is cylindrical shrinkage,  $\mathbf{C} = (-\cos \alpha, -\sin \alpha, 0)$  (Fig. 9b), for which  $\text{rot } \mathbf{C} = 0$ . This strain field does not cause the rotation of particles. This type may occur when a suspension is solidified in a capillary by cooling, whereby the consolidation develops from the capillary surface in a cylindrical manner. In actual practice, however, the cylindrical symmetry is not perfectly satisfied because an additional flow may occur due to the loss of volume upon shrinkage. If the matrix shrinks in a uniform manner, such as a uniform affine transformation (Fig. 9c), no particle rotation occurs. In our model, we assumed that the shrinking area is small compared to the particle size. If the area of uniform shrinkage is larger than the particle, not necessarily throughout the whole suspension, the chance of orientation deterioration might be reduced.

## Experimental

### Sample preparation

As-received powder of Dy123 (TEP Corporation, Tokyo, Japan) was further pulverized in a mill (Planetary Mono Mill PULVERISETTE 6, Fritsch GmbH, Idar-Obertein, Germany) with 100 zirconia balls of 15 mm in diameter in a 45 cm<sup>3</sup> zirconia vessel rotating at 100 rpm. Sixteen grams of Dy123 powder and 25 mL of ethanol were added to the vessel and milled for 5, 10, 20, and 30 h. During the milling process, the rotation was stopped for 1 min every 20 min to prevent a temperature increase.

### SEM observation

SEM images were collected using a scanning electron microscope (JSM-6510LV, JEOL Ltd., Tokyo, Japan) at an acceleration voltage of 20 kV.

### Preparation of the suspension

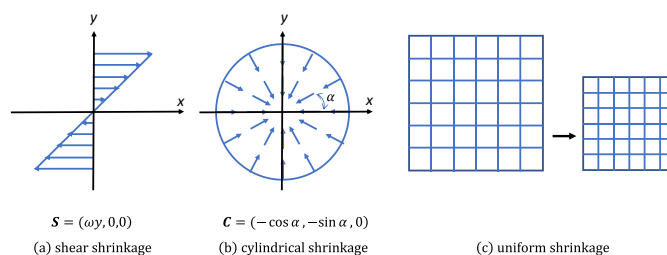


Fig. 9 Several types of shrinkage. (a) A shear type where  $\text{rot } \mathbf{S} \neq 0$ , (b) a cylindrical type where  $\text{rot } \mathbf{C} = 0$ , and (c) an affine-type uniform shrinkage upon which rotation does not occur.

A two-component epoxy adhesive, Araldite® Standard Huntsman, Japan, Kobe, Japan), composed of resin and hardener, was used for the suspension. A mixture of an equal volume of resin and hardener was prepared, and each of the milled Dy123 powders was immediately added to the mixture at a 1:10 weight ratio and mixed vigorously. The suspension obtained was poured into a glass capillary, and both edges of the capillary were sealed with clay (Chā-Seal, Kimble Chase Life Science and Research Products LLC, Vineland, NJ, USA) to obtain the sample for the X-ray diffraction measurement under a magnetic field.

### In-situ X-ray measurements

The capillary was set horizontally in the middle of the magnetic unit (KUχ10) generating a vertical 1 T static magnetic field. The magnetic unit was installed in the X-ray diffractometer (R-AXIS RAPID II, Rigaku Corp., Akishima, Japan) equipped with an imaging-plate area detector and graphite-monochromated MoKα X-ray source (0.71068 Å). The XRD measurement began about 10 min after preparation of the suspension of Dy123, and the X-ray was impinged for 600 s every 11.6 min while rotating the sample at 60 rpm. The measurement was performed at room temperature. The total experimental time was about 24 h.

### Data processing

The orientation of the  $\chi_3$  axis ( $\parallel b$  axis) was evaluated using FWHM of spots from the (200) and (006) planes. These spots have an almost identical  $2\theta$  of 21.0° and 21.4°, respectively, and show up at  $\beta = 90$  and 270° in the azimuth plot. The intensity between  $2\theta = 20.5$ – $21.8^\circ$  was integrated between  $\beta = 70.00$ – $110.00^\circ$  and  $\beta = 250.00$ – $290.00^\circ$ , respectively, using 2DP software from Rigaku Corp. (Akishima, Japan). The azimuthal  $\beta$  plot was performed, and the peaks obtained around  $\beta = 90$  and 270° were curve-fitted with the Lorentz function to obtain the FWHM using Igor Pro, WaveMetrics, Inc., Lake Oswego, OR, USA. The experimental results were compared with the theoretical prediction.

## Conclusions

The deterioration of the orientation of microcrystals in suspension during the curing process in a magnetic field was studied. To model the phenomena, it was assumed that shrinkage of the medium causes local shear strain, which

deteriorates the orientation already achieved. Based on this assumption, a model was proposed to predict the orientation degradation. According to the model, the orientation deterioration can be prevented by reducing the medium viscosity, the shrinkage rate, and the curing speed. For a given consolidation condition, there is an appropriate volume size that minimizes the orientation degradation; or given the particle size, there is a best choice of consolidation parameter set by which the orientation degradation is minimized. In-situ XRD measurements were performed on a mixture of Dy123 microcrystals and Araldite® to observe the deterioration in crystal orientation, and the experimental results were analyzed based on the model. The results were successfully explained by the model.

## Conflicts of interest

There are no conflicts to declare.

## Acknowledgements

This work was partly supported by the Adaptable and Seamless Technology Transfer Program through Target-Driven R&D (A-STEP), the Japan Science and Technology Agency (JST) and JSPS KAKENHI Grant Number JP17H03235.

## Notes and references

- M. Yamaki, S. Horii, M. Haruta and J.-i. Shimoyama, *Japanese Journal of Applied Physics*, 2012, **51**, 010107.
- N. Nakatsuka, H. Yasuda, T. Nagira and M. Yoshiya, 2009.
- I. Kvien and K. Oksman, *Applied Physics A – Materials Science & Processing*, 2007, **87**, 641-643.
- V. Timbrell, *Journal of Applied Physics*, 1972, **43**, 4839-4840.
- Jacopo Ciambella, David C. Stanier and S. S. Rahatekar, *Composites Part B*, 2017, **109** 129-137.
- G. Piao, F. Kimura, T. Takahashi, Y. Moritani, H. Awano, S. Nimori, K. Tsuda, K. Yonetake and T. Kimura, *Polymer Journal*, 2007, **39**, 589-592.
- C. Du, M. Li, M. Cao, S. Feng, H. Guo and B. Li, *Carbon*, 2018, **126**, 197-207.
- E. S. Choi, J. S. Brooks, D. L. Eaton, M. S. Al-Haik, M. Y. Hussaini, H. Garmestani, D. Li and K. Dahmen, *J. Appl. Phys.*, 2003, **94**, 6034-6039.
- F. Kimura and T. Kimura, *CrystEngComm*, 2018, **20**, 861-872.
- S. Tsukui, F. Kimura, E. F. Garman, S. Baba, N. Mizuno, B. Mikami and T. Kimura, *J. Appl. Cryst.*, 2016, **49**, 457-461.
- F. Kimura, W. Oshima, H. Matsumoto, H. Uekusa, K. Aburaya, M. Maeyama and T. Kimura, *CrystEngComm*, 2014, **16**, 6630-6634.
- T. Kimura, F. Kimura and M. Yoshino, *Langmuir*, 2006, **22**, 3464-3466.
- R. Kusumi, F. Kimura, G. Song and T. Kimura, *Journal of Magnetic Resonance*, 2012, **223**, 68-72.
- M. B. Roller, *POLYMER ENGINEERING AND SCIENCE*, 1975, **15**, 406-414.
- D. J. PLAZEK and J. Z. N. FRUND, *Journal of Polymer Science: Part B: Polymer Physics*, 1990, **28**, 431-448.
- James M. Rozell Jr., Greg W. Book, Jannette Cunningham, Clare Glorioso, Marcus Vlasse and J. P. Golben, *Physica C*, 1993, **204**, 384-388.
- S. Horii, T. Nishioka, I. Arimoto, S. Fujioka and T. Doi, *Supercond. Sci. Technol.*, 2016, **29**, 125007 (125006pp).
- S. Horii, A. Ishihara, T. Fukushima, T. Uchikoshi, H. Ogino, T. S. Suzuki, Y. Sakka, J.-i. Shimoyama and K. Kishio, *Sci Technol Adv Mater*, 2009, **10**, 014604.
- Y. He, Doctor of Philosophy, Ph.D. thesis, The University of Michigan, 2019.
- C. Tsuboi, S. Tsukui, F. Kimura, T. Kimura, K. Hasegawa, S. Baba and N. Mizuno, *Journal of Applied Crystallography*, 2016, **49**, 2100-2105.
- F. Perrin, *J. Phys. Radium*, 1934, **5**, 497-511.
- T. Kimura, M. Yamato, W. Koshimizu, M. Koike and T. Kawai, *Langmuir*, 2000, **16**, 858-861.
- G.D. Chryssikos, E.I. Kamitsos, J.A. Kapoutsis, A.P. Patsis, V. Psycharis, A. Koufoudakis, Ch. Mitros, G. Kallias, E. Gamari-Seale and D. Niarchos, *Physica C*, 1995, **254**, 44-62.
- J. F. Nye, *Physical properties of crystals: their representation by tensors and matrices*, Oxford university press, 1985.
- K. Matsumoto, F. Kimura, G. Song, S. Yamane, H. Kikuchi, T. Tanaka, S. Higuchi, N. Kitamura and T. Kimura, *Cryst. Growth Des.*, 2014, **14**, 6486-6491.
- H. A. Materials, *Araldite Standard Two component epoxy adhesive*, 2011.
- Lolei Khoun and P. Hubert, *POLYMER COMPOSITES*, 2010, **2010**, 1603-1610.
- J.A. Ramos, N. Pagani, C.C. Riccardi, J. Borrajo, S.N. Goyanes and I. Mondragon, *POLYMER ENGINEERING AND SCIENCE*, 2005, **46**, 3323-3328.
- Ross F. Minty, James L. Thomason, Liu Yang, Walter Stanley and A. Roy, *Polymer Testing*, 2019, **73**, 316-326.
- Ken Oota and M. Saka, *POLYMER ENGINEERING AND SCIENCE*, 2001, **41**, 1373-1379.
- J. D. Livingston, J. H. R. Hart and W. P. Wolf, *J. Appl. Phys.*, 1988, **64**, 5806-5808.
- Z. Hiroi, M. Takano, Y. Takeda, R. Kanno and Y. Bando, *Japanese Journal of Applied Physics*, 1988, **27**, L580-L583.
- Fumiko Kimura, Shigeru Horii, Itsuki Arimoto, Daisuke Notsu, Toshiya Doi, Masahisa Wada and T. Kimura, *CrystEngComm*, 2019, **21**, 4221-4227.

